Velocity estimation by the CRS method: A GPR real data example

H. Perroud, M. Tygel and S. Bergler

email: *Herve.Perroud@univ-pau.fr*
keywords: *GPR, CRS, rms-velocity, interval velocity*

ABSTRACT

Perroud, Tygel and Bergler *describe the use of the Common Reflection Surface (CRS) method to estimate velocities from Ground Penetrating Radar (GPR) data. Applied to GPR multi-coverage data, the CRS method provides, as one of its outputs, the time-domain rms-velocity map that is then converted to depth by the familiar Dix algorithm. Combination of the obtained depth-converted velocity map with in situ measurements of electrical resistivity enables to estimate both water content and water conductivity. These quantities are essential to delineate infiltration of contaminants from the surface after industrial or agriculture activities. The method has been applied to a real dataset and compared with the classical NMO approach. The results show that the CRS method provides a much more detailed velocity field, thus improving the potential of GPR as an investigation tool for environmental studies.*

INTRODUCTION

The CRS method is a novel seismic time-imaging technique that provides also attributes related to the subsurface model. These attributes, expressed in terms of wavefront curvatures and emergence angle, can be combined to estimate the RMS velocities within the illuminated part of the subsurface model. The purpose of this paper is to investigate the ability of the CRS method to retrieve RMS velocities (together with their corresponding interval velocities), as compared with the classical common-midpoint (CMP) and normal moveout (NMO) approach. For the comparison, we use a real dataset obtained from a near-surface GPR multi-offset survey. In this way, the ability of the CRS method to handle the specificities of electro-magnetic waves can be assessed, such as unusual scaling and medium attenuation. Furthermore, the interval velocities, obtained after conversion of the GPR velocities, are combined with parallel electrical resistivity measurements to recover ground-water properties such as water-content or water conductivity. This combination allows for a better understanding of the physical meaning of the original GPR velocities, as obtained by the CMP/NMO and CRS procedures. Finally, as the GPR experiments were repeated in time, we shall be able to monitor the stability of these velocity determinations.

There are three main factors that contribute to the bulk conductivity in a porous soil, namely the water content, the water conductivity, and the clay content, provided that the matrix can be considered as insulating. For environmental issues such as the monitoring of contaminant infiltration, one important objective is to evaluate the water conductivity, mainly in the vadose zone between the surface and the aquifer nappe, where the water content is highly variable. As a consequence, we need independent measurements, so as to separate the effect of these parameters. Following the strategy proposed in Garambois et al. (2002), we use, as a first step, GPR velocity to estimate water content. As a next step, we combine the obtained results with the electrical resistivity measurements to delineate water conductivities anomalies. The anomalies that remain stationary in time will be attributed to clay, while the ones that vary with time will be interpreted as an evidence for the diffusion of a solution in the ground water. It is thus of primary importance to get the most detailed and reliable GPR velocity field estimation. To make it feasible in an industrial context, the whole procedure is required to be easily implemented and processed. This means that the experimental

setup should be simple and the data processing should be as automated as possible.

In the first section, we give an overview of the CRS method and literature, so that the reader can find the main concepts needed to understand the presented arguments and results. In particular, we discuss various important aspects related to the use of the CRS method (such as the selection of apertures) as well as the interpretation of the CRS results, in contrast to the classical NMO process. For a detailed description of the CRS method we refer to Mann (2002). We next present the GPR multi-offset experiment, and the dataset used in this investigation. Using this dataset, we describe, in the following two sections, how both classical NMO and CRS are used to estimate the RMS velocities. Finally, we evaluate the geophysical significance of the obtained velocity fields, by combining them with electrical measurements and deriving the sought for ground-water properties.

CRS TIME-IMAGING OVERVIEW

The classical common-midpoint (CMP) method is a routine step in seismic processing to obtain a (time-domain) velocity distribution of the subsurface, as well as a simulated (stacked) zero-offset section. The obtained time-domain velocities can be next converted to interval velocities in depth, thus providing a subsurface velocity model that is needed for a number of applications. For the historic description of the CMP method, as well as practical developments, the reader is referred to Yilmaz (2000) and references given there.

Considering a 2D-situation in which all source and receivers belong to a single seismic line, the CMP method is based on two main steps. First, the data are sorted out into CMP gathers. Each CMP gather is determined by the fixed CMP location, x_0, and by the ensemble of source-receiver pairs (S, G), located by the coordinates $(x_0 - h, x_0 + h)$, where h is the (variable) half-offset. Second, a coherence analysis is carried out at each sample, t_0, on the ZO trace that is to be constructed at the CMP location, x_0. A widely used coherence measure is semblance (Neidell and Taner, 1971) to which we refer to throughout the paper. The coherence analysis is to be applied using the traveltime normal moveout (NMO), given by the hyperbolic traveltime expression

$$t^2_{\mathrm{CMP}}(h) = t_0^2 + \frac{4h^2}{v^2_{\mathrm{NMO}}} \ . \tag{1}$$

In the above expression, v_{NMO} is the velocity that yields the best coherence (semblance) to the data. For this reason, $v_{\mathrm{NMO}} = v_{\mathrm{NMO}}(t_0, x_0)$ is now referred to the NMO velocity associated to the ZO (central) location point, x_0 and time sample, t_0. After the determination of the NMO velocity, the so-called normal-moveout is applied to the data using the traveltime expression (1), and then the data are stacked to constitute a simulated ZO section. In practice, particularly in the presence of significant reflector dips, the procedure outlined above is further refined upon the introduction of dip moveout (DMO) together with the previous NMO transformation. We refer once again to Yilmaz (2000) for a detailed discussion on these topics. We also mention that the cascaded NMO/DMO transformations can be alternatively replaced by the transformation called migration to zero-offset (MZO), see, e.g., Tygel et al. (1998).

As seen from the previous discussion, the CMP method, although widely used in practice, has two main limitations: (a) It uses only CMP data for the coherency analysis. This means that much of the available data (from source and receivers not symmetrically located around the CMP) are not being used and (b) The only attribute that is extracted from the data is the NMO velocity. If the NMO correction, whose expression is time-dependent, is carried out due to a NMO velocity distribution obtained on the basis of picks in the semblance map, artifacts, known as NMO stretch, are introduced. This is, however, a commonly applied approach and also discussed later on.

Due to the significant reduction of the costs for quality-data acquisition and computing power in the recent years, geophysicists are being able to overcome the limitations of the CMP method, for example, by the use of more general traveltime moveout expressions. These can account and stack the contributions within an extended gather that consists of arbitrary source-receiver locations around a central point. The central points can, of course, be taken at an old CMP location.

In the recent literature, those methods that are based on more general traveltime moveouts, together with multi-parametric search strategies to estimate and apply the various traveltime attributes, are referred

to as "macro-model independent reflection imaging". A collection of important contributions to the subject is provided in Hubral (1999)[1].

In the present 2D-situation, it can be shown that the second-order traveltime of a primary reflection for a source and receiver pair whose midpoint is arbitrarily located in the *vicinity* of a central point, depend on three parameters, all of them connected with the primary ZO ray that refers to that point[2].

The dependence on more parameters implies that one has to use a more involved coherency method to retrieve the required traveltime attributes, as opposed to the simple single-parameter semblance analysis utilized in the CMP method. At first, this might be seen as a disadvantage because of the enhanced computational effort that is implied when three attributes (instead of one) are to be estimated. A second consideration, however, realizes that the new attributes provide more information that can be used for better imaging, as well as for a better determination of the velocity model as needed, for example in migration. Investigations are currently been made on the use of CRS attributes for the inversion of a macro-model. Initial results are reported in Biloti et al. (2002) and Duveneck and Hubral (2002).

The Common Reflection Surface (CRS) method is one of the generalizations of the classical CMP method in the sense described above[3]. It uses the hyperbolic traveltime moveout, here written in the appealing form

$$t_{\text{hyp}}^2(x_{\text{m}}, h) = \left[t_0 + \frac{2 \sin \alpha}{v_0}(x_{\text{m}} - x_0) \right]^2 + 4 \left[\frac{h^2}{v_{\text{NMO}}^2} + \frac{(x_{\text{m}} - x_0)^2}{v_{\text{PST}}^2} \right] . \tag{2}$$

Formula (2) considers three fixed (central) quantities, namely, x_0, t_0 and v_0. The coordinate, x_0, specifies the (central) point x_0 on the seismic line at which a coincident source and receiver pair, $S_0 = G_0 = x_0$, is located. The central traveltime, t_0, represents the ZO primary-reflection traveltime that pertains to the central point, x_0. Finally, v_0 denotes the velocity of the medium at the central point, x_0. Now, (x_{m}, h) denote the midpoint and half-offset coordinates of an arbitrary source-receiver pair, (S, G), in the vicinity of the central point, x_0. In other words, the source and receiver distances to the central point x_0 are given by $(x_{\text{m}} - h - x_0, x_{\text{m}} + h - x_0)$. For any given midpoint and half-offset co-ordinates, (x_{m}, h), that specify a source, S and a receiver, G, that are in the vicinity the central point, x_0, $t_{\text{hyp}}(x_{\text{m}}, h)$ provides the hyperbolic approximation of the traveltime along the primary-reflection ray that connects S to G.

The hyperbolic traveltime (2) depend on three parameters or attributes, α, v_{NMO} and v_{PST}. Here, v_{NMO} is the familiar NMO velocity that appears in the CMP method. This is no surprise, since, for the situation of a CMP gather, namely, source-receiver pairs, (x_{m}, h), in which $x_{\text{m}} = x_0$, the general expression (2) reduces to its CMP counterpart given by equation (1). The parameter, α, represents the emergence angle of the ZO (central) ray at x_0. To understand the last attribute, v_{PST}, we consider the situation of a ZO gather, namely, source and receiver pairs (x_{m}, t_m) in which $h = 0$. In this case, the hyperbolic expression reduces to

$$t_{\text{hyp}}^2(x_{\text{m}}, h) = \left[t_0 + \frac{2 \sin \alpha}{v_0}(x_{\text{m}} - x_0) \right]^2 + \frac{4(x_{\text{m}} - x_0)^2}{v_{\text{PST}}^2} . \tag{3}$$

We see that, except for the time-shift, $t_{\text{shift}} = 2(\sin \alpha / v_0)(x_{\text{m}} - x_0)$, inside the parenthesis, formula (3) has the same form than the corresponding NMO traveltime. In this way, the velocity attribute, v_{PST}, referred to the ZO situation, plays the same role as the NMO velocity, as defined by the CMP situation. Since, in practice, the (non-available) ZO section is derived (simulated) from the CMP traveltimes by stacking, we find convenient it to refer the quantity, v_{PST}, as the post-stack-velocity attribute of the hyperbolic traveltime.

---

[1]The terminology *macro-model independent reflection imaging* intends to indicate that the extraction of attributes and stacking procedures are designed to be less dependent on an a priori given macro-velocity model. As a previous knowledge of the velocity model is always welcome, many geophysicists prefer to use the alternative terminology *data-driven reflection imaging*.

[2]Here, the term *vicinity* is not to be understood as "very close", but such as the zero-order ray theory description holds. The actual aperture depends on various factors such as the main frequency of the source pulse and the ratio between the source-receiver offset (aperture) and the reflector's depth.

[3]In the literature of macro-velocity independent or data-driven seismic reflection imaging methods, the Multifocus method (introduced by Gelchinsky and co-workers), the Polystack or shifted-hyperbola method (introduced by de Bazelaire and co-workers) and the common-reflection (CRS) method (introduced by Hubral and co-workers and developed by the WIT Consortium) occupy a preeminent role. The reader is once again referred to Hubral (1999) for a brief survey and applications of these methods.
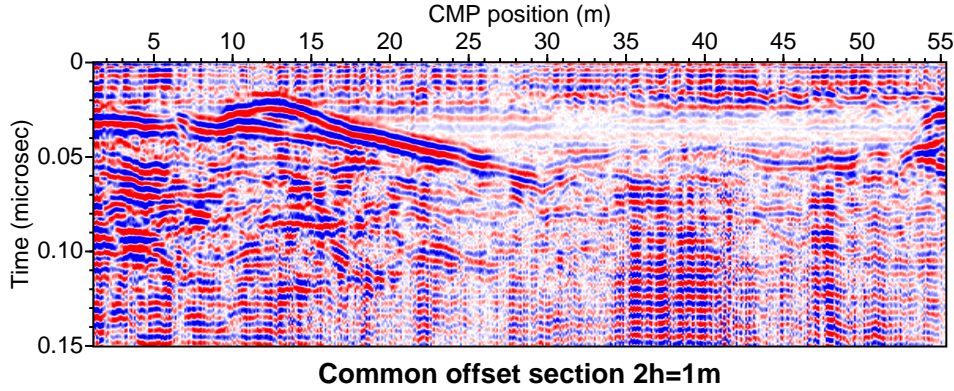
Figure 1: Example common offset section for offset 2h=1m

Please note, for a seismic line on a plane measurement surface v_{NMO} and v_{PST} are expressible in terms of wavefront characteristics, namely the angle α as well as the wavefront curvatures K_{NIP} and K_N of two hypothetical waves (Hubral, 1983). In this case, the hyperbolic traveltime formula (2) reads as given in, e.g., Tygel et al. (1997) and Jäger et al. (2001). However, in the following sections these wavefront characteristics are not explicitly used but v_{NMO}. We therefore prefer the hyperbolic traveltime as given in equation (2).

All fixed quantities, x_0, t_0 and v_0 are supposed to be given for the application of the CRS process. Note also that each central co-ordinate, x_0, locates a trace of the simulated ZO section to be constructed. The velocity, v_0, is the surface velocity for that trace. Finally, each time, t_0, can be consider as a time sample in the construction of the trace at x_0. The CRS stacking is done taking each time sample at a time.

As a result of the CRS method, one obtains the following functions (sections) defined on the grid points, (x_0, t_0) of ZO trace locations (for example, CMPs) and ZO time samples: (a) The stacked value (ZO simulated section); (b) the coherence value of the stack; (c) the NMO velocity section, $v_{\mathrm{NMO}}(x_0, t_0)$; (d) the angle section, $\alpha(x_0, t_0)$ and (e) the PST velocity, $v_{\mathrm{PST}}(x_0, t_0)$. By means of the relationship

$$v_{\mathrm{rms}} = v_{\mathrm{NMO}} \cos \alpha \approx v_{\mathrm{NMO}}(1 - \alpha^2/2) \,, \tag{4}$$

between the root-mean-square (RMS) velocity, v_{rms} and the NMO velocity, v_{NMO}, we readily obtain, as a simple additional product, the RMS-velocity section, namely, $v_{\mathrm{rms}}(x_0, t_0)$. It can be easily seen that if α is small enough (say less than $20°$), the two quantities v_{NMO} and v_{rms} can be identified within reasonable precision. This situation holds in this case study and the $v_{\mathrm{NMO}}/v_{\mathrm{rms}}$ section is of most importance for the application we envisage in this work.

THE GPR DATASET

Multi-coverage GPR dataset is not common, since most acquisition systems have only one channel. GPR investigation is therefore usually conducted in a single common-offset configuration. In the same way as in seismics, the GPR method provides a time image of the subsurface (electromagnetic) reflectors and diffractors. For migration or depth conversion purposes, a few CMP experiments are, in general, also made, the obtained velocities being interpolated between them. Due to a new generation of multi-channel instruments, GPR investigation practices are changing to use their improved capabilities. In this study, we used a Ramac-2 4 channels control unit manufactured by Mala Geophysics, together with 2 pairs of unshielded 200 Mhz antennas. The multi-offset coverage data were obtained by repeated profiling with the 4 antennas mounted on a PVC cart with varying spacings. Altogether, we obtained 28 different offsets, every 0.2 m from 0.6 to 6 m, for each CMP spaced every 0.1 m on a 55 m long profile. The traces were sampled over 0.15 microseconds, what corresponds roughly to a 6 m penetration depth for a mean velocity
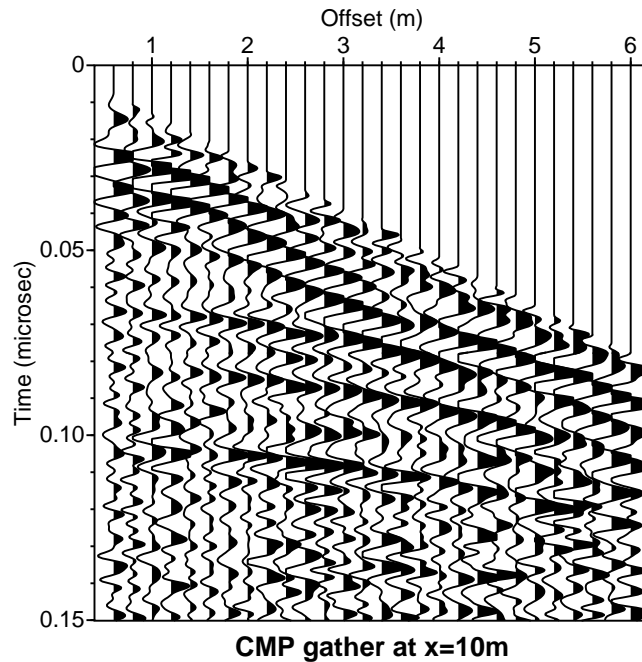
Figure 2: Example common mid-point gather for position x=10m

of $0.75 10^8$ m/s. These procedures were repeated over time to monitor the changes in the subsurface water properties. In this on-going project, we plan to achieve a full-year coverage at a one-month time interval.

Standard processing was applied to the datasets, including static shift for zero time, mean amplitude removal, tapered bandpass filtering, mute of air wave, and amplitude balancing through a division of each common-offset gather by the mean of its envelope traces. The final datasets were then sorted in CMP number for velocity estimation and stacking. As an example, one common-offset section is shown in Figure 1. It presents clear reflection events but also artifacts (ringing) due to the interaction between antennas in our multi-offset configuration. It can be noted that the time is given in microseconds, and distance in meters. The scales that are used lead to a vertical exaggeration of apparent dips by a factor of more than 3. Furthermore, the maximum CMP aperture reaches a value of 5 for the uppermost reflections, down to less than 1 for the lowermost ones. A typical common mid-point (CMP) gather is shown in Figure 2. It reveals a series of coherent hyperbolic reflection-time curves that should allow a precise determination of the GPR velocity field. Note that the artifacts mentioned above appear uncorrelated from trace to trace.

On the same profile, an electrical resistivity section was obtained with a 64-electrodes Syscal-R2 system from Iris Instruments, with electrode interval of 1 m. Measured apparent resistivities were converted into a 2D resistivity section using the inversion algorithm of Loke and Barker (1996), with random residuals less than a few percents. The obtained resistivity section, shown in Figure 3, reveals both vertical and lateral variations. As shown below, these provide interesting comparisons with our GPR velocity estimations.

RMS VELOCITY ESTIMATION WITH CLASSICAL NMO

The procedure followed here to derive the velocity field involves, in a first step, a classical NMO velocity analysis, performed with the aid of the SU seismic processing software. Semblance maps were computed for a selection of CMPs, spaced every 2m along the whole profile. For these, semblance maxima were, then, manually picked for each reflection-time curve. In a second step, to overcome the imprecision of the picking due to the elongation of the semblance maxima along the velocity axis, the previously obtained velocities were refined by a means of visual adjustment of the corresponding hyperbolae on the CMP data. This is possible only when the signal-to-noise ratio of the analyzed event is significantly higher than 1, what
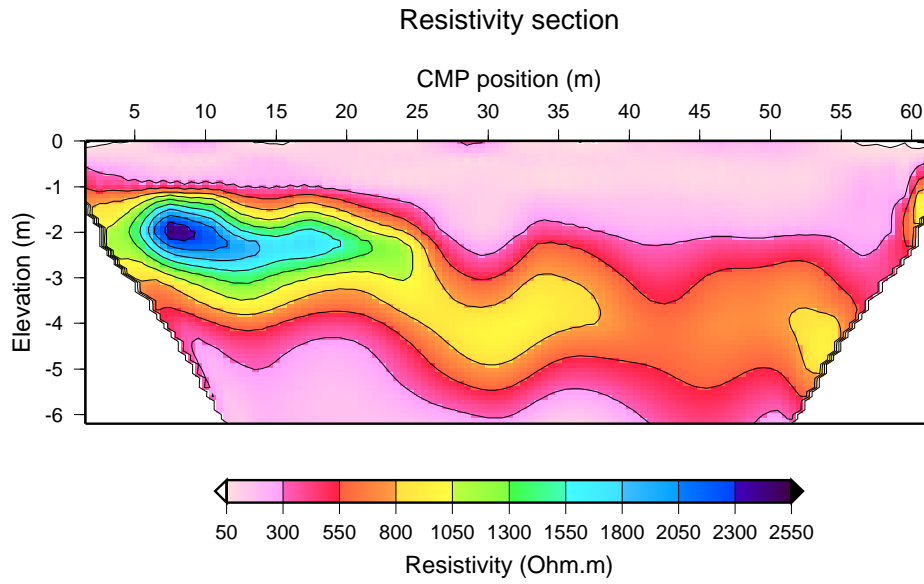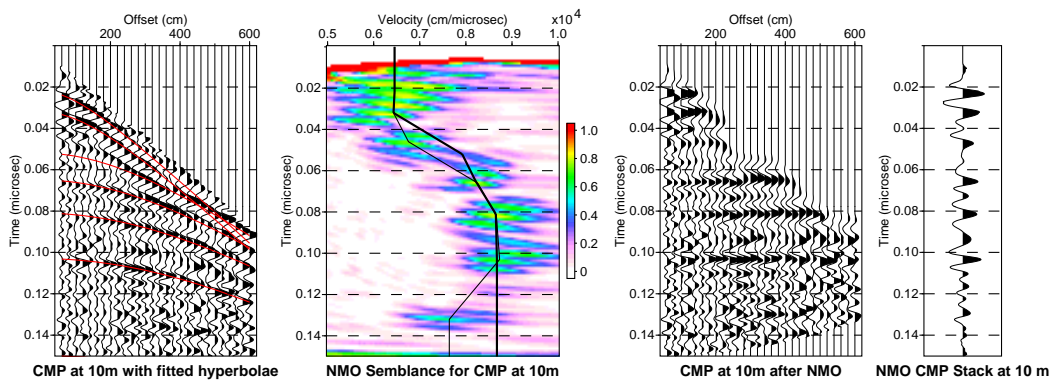
Resistivity section

Figure 3: Electrical resistivity section

Figure 4: Example of velocity analysis for the CMP at 10m

Classical NMO Vrms

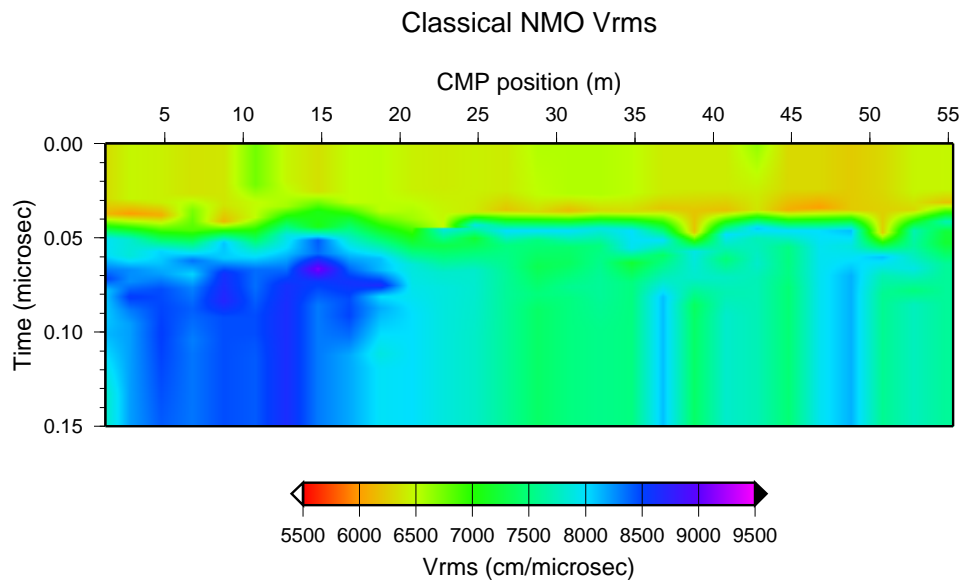**Figure 5:** v_{rms} velocity field obtained by the classical NMO method
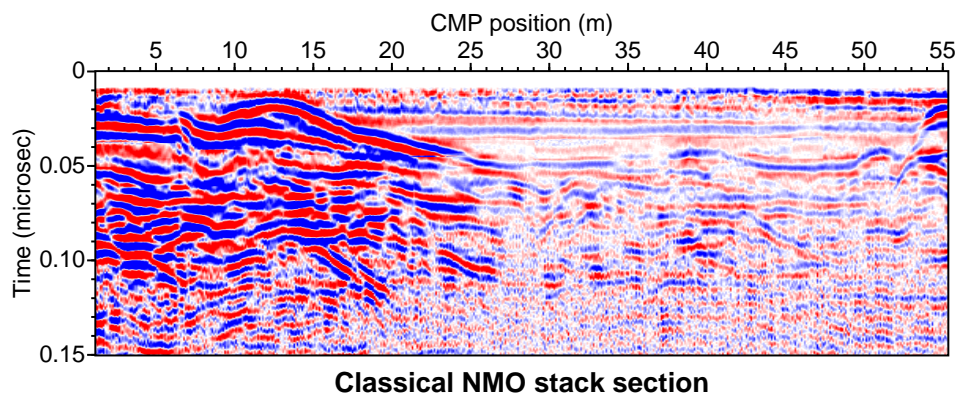

Figure 6: Stack section obtained by the classical NMO method, using the velocity field of Figure 5

is not achieved everywhere in the section. An example of such a velocity estimation is given in Figure 4, for the CMP located at the position 10m along the profile.

The final time-velocity law, shown as the black thick line on top of the semblance map, was obtained after several iterations of hyperbolae fitting from the initial time-velocity law, shown as the thin black line. It leads to the NMO corrected CMP gather, where all events appears quite horizontal, and the corresponding stacked zero-offset trace. In this example, some peculiarities of the GPR data can be recognized. First, we note the change of polarity along the third event, corresponding to a change of sign of the reflection coefficient with increasing incidence angle. Second, due to the large aperture, the NMO correction gives rise to very severe stretches for the uppermost events, these being, for that reason, largely muted. In fact, the implementation of the SU velocity analysis assumes a limit (upper bound) of the acceptable stretch induced by the NMO. We fixed this limit to a factor of 1.5 (that is a 50% stretch), namely, samples with larger stretch were simply muted. This implicitly generates a restriction to the number of traces to be used in the procedure, since the NMO stretch is directly dependent upon the CMP aperture for fixed offset and velocity (see details below). Finally, one can observe that a clear maximum in the lower part of the semblance map (at time 0.13 microsec), although initially picked, was later rejected since it would lead to a unacceptable low velocity, which, in turn, would convert into a physically impossible interval velocity.

From the set of recovered time-velocity laws spaced along the profile, a bilinear interpolation was applied to generate a complete velocity map, namely one that is defined for all time samples and all midpoints. The obtained RMS velocity field is shown in Figure 5, together with the corresponding stacked section in Figure 6, which provides already a much better subsurface image that the one shown in Figure 1. We shall come back to this velocity field later, after the presentation of the corresponding one obtained by the CRS method, as described in the following section.

RMS VELOCITY ESTIMATION WITH THE CRS METHOD

The CRS software used in this part corresponds to version 4.2, from the University of Karlsruhe. To efficiently implement the three-parameter search, as required by the CRS method, it comprises four successive steps, the first three being one parameter searches confined to specific gathers, followed by a final optimization step:

- a first search, named *automatic CMP stack*, is made in the CMP gather. In a similar way as in the NMO approach, it yields to a first estimation of parameter v_{NMO}. An important difference, however, is that, as opposed to the NMO manual visual procedure, the CRS stack is made fully automatic for every sample and every CMP that pertains to the zero-offset section to be constructed. The automatic search requires the selection of a parameter value which maximizes the coherence criteria. To avoid a bias on the v_{NMO} parameter due to the the validity range of the second-order (hyperbolic) reflection-time approximation, the offset aperture must be controlled (restricted) in the CMP gather. Namely, offsets exceeding the chosen aperture are not included in the search. The choice of the aperture that is used is selected by the user. As discussed below, an adequate choice of the offset aperture is crucial for best parameter estimation and stack results. After the determination of the v_{rms} parameter at each CMP location and for every traveltime sample, an output stacked section is constructed. In the same way as in the NMO procedure, this stacked section is considered as a simulated zero-offset section.

- The zero-offset section build in the first step is next used for a search of parameter α, the emergence angle. It uses the first-order (linear) plane-wave approximation of the zero-offset traveltime in a small mid-point aperture range.

- Once α has been estimated, the search of the third parameter, v_{PST} is conducted, also in the stacked section. It uses, this time, the full second-order (hyperbolic) approximation of the zero-offset traveltime within a mid-point aperture. This aperture is also user defined. After the above three steps, a new section, called the *initial CRS stack* is obtained by stacking all the input data, within an aperture of elliptical shape in the midpoint-offset plane, using the full 2D CRS stacking surface as given by equation 2.

- Finally, three-parameter optimization scheme is applied to the full input data. The optimization scheme uses the previous estimations of the parameters as initial values. The optimized parameters

can then be seen as a *refinement* of the previous ones, that were obtained using three independent one-parameter searches. Using the optimized attributes, a new stacked section, the called *optimized CRS stack*, as well as the corresponding coherence (semblance) section, are obtained. As a further result, a Kirchhoff-type time-migrated section can also be readily constructed.

As can be seen from this short presentation, there is a recurrent need for the CRS application to limit the extent of the data to be analyzed or stacked, so as to insure the good precision of measured parameters. In the classical NMO approach, this is implicitly achieved by limiting the stretch effect induced by the NMO correction to a chosen threshold (in our case study this value was taken to be 1.5). As the CRS method suffers from no stretch, there should be some preliminary assessment of the apertures (both in offset and mid-point axes) to be used before running the software.

CRS apertures

The first parameter to be estimated by the CRS method is the v_{NMO} velocity. Similarly to the NMO method, the v_{NMO} parameter is obtained by a one-dimensional search applied to the CMP gather. More specifically, for a fixed CMP location, x_0, and each time sample, t_0, the search is done in the offset, domain, namely, for varying h. A necessary requirement is then to define the maximum offset that will be used. Obviously, this will depend upon the time sample itself. In the present implementation, CRS requires that two points are given in the offset-time (x_0, t_0)-plane, to draw a linear offset limit between them. Furthermore, to avoid strong edge effects, a tapered zone is also implemented within this limit.

To establish a fair comparison with the classical NMO approach, we try first to choose the CRS offset aperture so that it corresponds to the previously chosen NMO stretch mute ratio (1.5), although the CRS does not generate a stretch. To achieve this, we derive from expression (1) the following short formula, in the horizontal and constant velocity case, between the offset aperture, defined as the tangent of the reflection semi-angle, and the NMO stretch effect, for a given offset and velocity:

$$\mathrm{NMO\_stretch} = \frac{\mathrm{d}t_0}{\mathrm{d}t} = \sqrt{1 + \mathrm{aperture}^2} \; , \tag{5}$$

We can thus estimate that the maximal stretch ratio of 1.5, used in the NMO processing above, corresponds to a maximal aperture of 1.12. The corresponding maximal offset can then be obtained for any travel-time t with the linear expression:

$$\mathrm{offset\_max} = \frac{v_0.\mathrm{aperture}}{\sqrt{1 + \mathrm{aperture}^2}} t \; , \tag{6}$$

For the exemplary CMP at 10m, the corresponding line is shown in blue on top of the reflection events in the left part of Figure 7. Unhappily, the CRS software does not use this definition of aperture. To tell CRS not to use the offsets beyond that line, we have to determine the two points which limit the CRS offset aperture so that the same data samples will be kept for analysis. This is not straightforward, since these two points are defined in the CRS code by ZO time and offset pairs, while the CMP gather axes are real travel-time and offset. An initial guess of v_{NMO} (middle-left part of Figure 7) is therefore necessary to adjust these two points as shown by the red line in Figure 7, fitted on top of the previous blue line. The second red line inside the offset aperture range corresponds to the beginning of the tapered zone, chosen here at 90% of the defined aperture. After applying the CRS moveout, we obtain the new gather shown in the middle-right part of Figure 7. Finally, the corresponding stacked trace is shown on the right part of Figure 7. It can be seen by comparison with the NMO corrected CMP gather shown in Figure 4 that the CRS offset aperture so-defined is very similar to the NMO stretch mute ratio of 1.5 used above. Due to the absence of stretch, the CRS CMP stacked trace appears less smooth, and has more contrasted amplitudes, than the NMO stacked trace.

It should be well understood that we could have used in CRS a somewhat larger aperture than in NMO, since it has no stretch effect. To verify this, we did run again the CRS with maximum apertures of 1.5 and 2 instead of 1.12, for the exemplary CMP at 10m. Results are shown after the first automatic CRS moveout in Figure 8 and 9 respectively. It can be observed that, even for the bigger aperture, the flattening of the reflection events is still quite good, and no clear sign of inaccuracies in the traveltime approximation
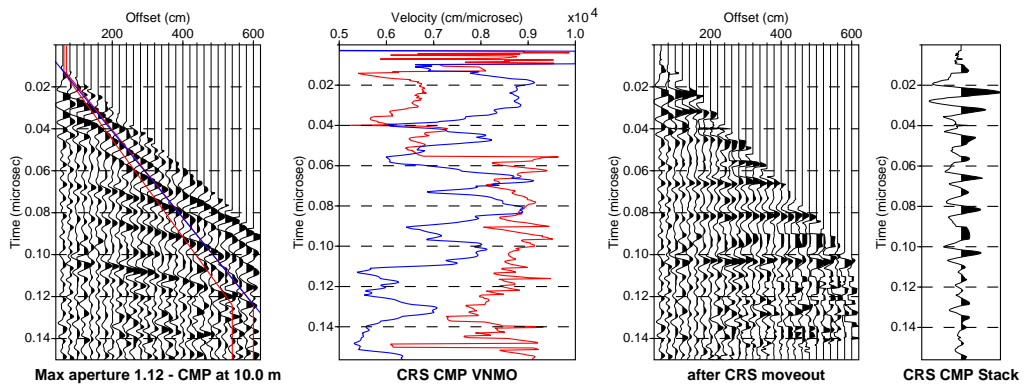
Figure 7: Left: offset aperture for the CMP at 10 m; the blue line corresponds to a maximum aperture of 1.12, while the red lines are the limits of the tapered zone for the CRS offset aperture. Middle-left: first v_{NMO} estimation (red line) leading to best coherency (blue line) in the CMP gather; Middle-right: same gather after CRS moveout using the shown v_{NMO}. Right: corresponding stacked trace
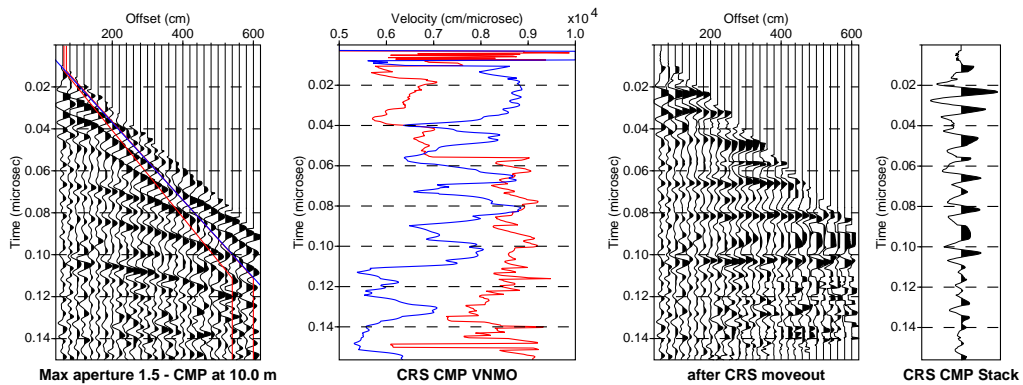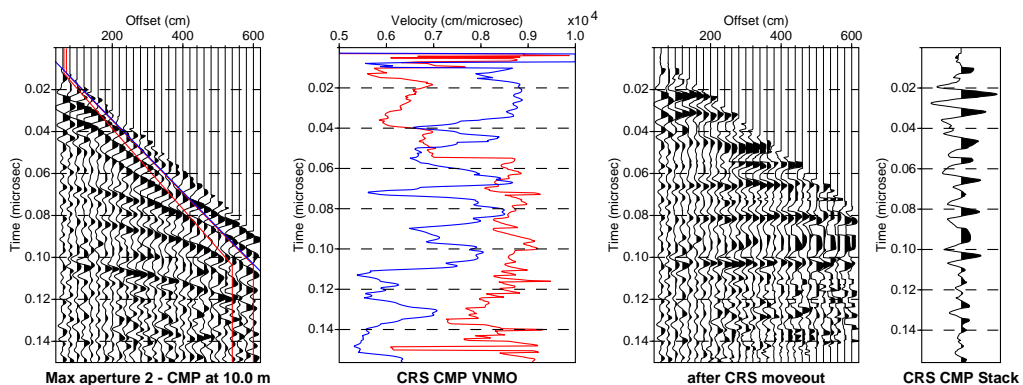

Figure 8: same as Figure 7, for an offset maximum aperture of 1.5

Figure 9: same as Figure 7, for an offset maximum aperture of 2
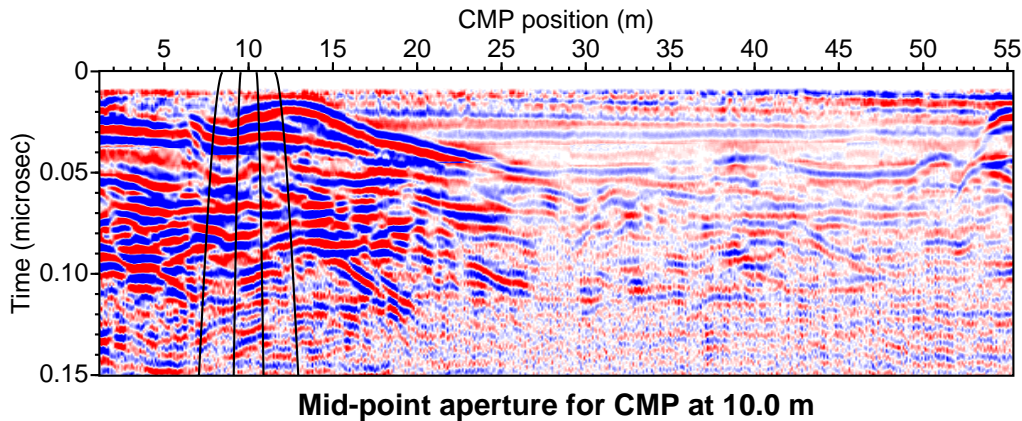
Mid-point aperture for CMP at 10.0 m

Figure 10: Mid-point aperture for the CMP at 10 m; the black lines are the limits of the CRS mid-point aperture for first-order linear (inner curves) and second-order hyperbolic parameter searches (outer curves)

appeared, due to higher-order terms. The absence of stretch allows therefore to use a larger part of the reflection events, what should be specially significant for the uppermost events, or for those of low signal-to-noise ratio (see around time 0.06 microsec for example).

The mid-point aperture used for the following steps of the CRS parameter searches implements a time-variable Fresnel zone related search domain, within limits that have to be explicitly defined. The minimal value has to be large enough to allow parameter searches for the uppermost events, it was chosen here to 1.5m, that corresponds to 15 CMP intervals. The aperture then increases with time, as would a Fresnel zone width for increasing depth, until it reaches the maximal value of 3m. For the plane-wave angle estimation, that aperture is reduced by a factor of 0.3. These mid-point aperture limits are superposed on top of a zero-offset simulated section, here obtained by the classical NMO approach in the previous section (Figure10). It should be noted that the CRS approximation assumes implicitly that the reflecting interface can be locally represented by an arc of circle (Höcht et al., 1999), where the reflection points of the analyzed source-receiver trajectories are allowed to spread. It seems thus worthwhile that the chosen mid-point aperture is large enough to fully include such an arc of circle, but not much more. In our case, the chosen mid-point aperture presents such a characteristic.

Automatic CMP attributes and stack

For all subsequent CRS calculations, we shall use the median offset aperture of 1.5, which appears above as a good compromise between the acceptable stretch effect of the NMO and the inevitable large offset inaccuracies of the second-order approximation used in the stretch-free CRS. Together with the parameters estimations and simulated stack section, the CRS software provides also some indications of the quality of these determinations. We shall use here two of them, first the measure of the best coherence, and second the number of traces used. As a matter of fact, attributes are estimated for all time samples, whether there is a reflection event or not. It appears thus necessary to *clean* the CRS parameters estimations before using them, that is to remove all values obtained with a coherence lower than a chosen threshold. By examining Figures 7 to 9, which show the coherence measures for the exemplary CMP at 10m, a simple time-invariant threshold does not seem adequate, since it would accept coherence troughs for short times, while rejecting coherence peaks for long times. We therefore implement a variable threshold, linearly decreasing with time between a high value (0.5) defined for a short t_0, and a low value (0.2) for a long one, and extrapolated over the whole trace, as shown in Figure 11. The second adjustment we made is related to the number of traces used in the parameter search, which is a function of the offset aperture discussed above. If the number of traces is too low, what happens in the shorter times, the coherence measure is meaningless. We choose here to reject all parameters obtained with less than 4 traces (for a maximum of 28 in each CMP gather in
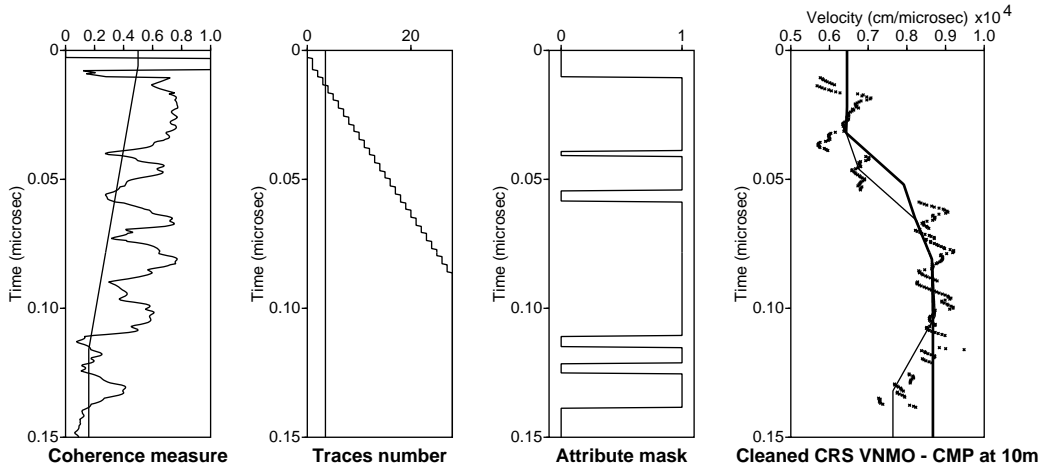
Figure 11: Left: CRS CMP autostack coherence measure for the exemplary CMP at 10m, with the time-variable threshold used to remove meaningless attribute values; Middle-left: Number of traces used and its threshold; Middle-right: Mask corresponding to the combination of the two selection criteria; Right: Cleaned CRS CMP autostack v_{NMO}, compared to both initial (thin line) and final (thick line) NMO derived stacking velocity laws

our dataset). After application of these two criteria, we obtained the *cleaned* v_{NMO} velocity law displayed in Figure 11, that can be compared with the classical NMO derived velocity laws obtained in the previous sections (both initial and final). As expected due to the strong similarity between this first CRS step and the classical NMO, the cleaned CRS v_{NMO} velocity law is very similar to the initial NMO velocity law obtained by manually picking maxima in the semblance map. It can be noted in particular that the anomaly coherence maxima (at time 0.13 microsec) already seen in the NMO approach is also automatically picked by the CRS in the CMP gather.

As stated above, the main difference up-to-now between the two approaches is that the CRS code picks automatically the best stacking velocity, for all time samples and all CMPs. While this difference seems at first glance secondary, or a matter of implementation, it is in fact a really important one since it leads not to one velocity estimation for a given reflection event, but to a set of velocity estimations for all time samples that constitute it. This effect can be clearly seen in the comparison of the NMO manually-picked velocities and the CRS automatic ones, as shown in Figure 11 for our exemplary CMP at 10m. It will lead us to include later a regularization process of the CRS v_{NMO} velocity field, before conversion to interval velocities.

According to the changing characteristics of the dataset between the left and right parts of the investigated area, we had in fact to split the dataset in two parts that were cleaned with slightly different threshold laws, and subsequently merged. This first CRS step leads to the cleaned v_{NMO} and zero-offset (stacked) sections that are shown in Figures 12 and 13. They are directly comparable to the ones obtained by the classical NMO approach (Figures 5 and 6). However, they are intermediate output sections, that can be used for on-going processes or quality control, but they do not include essential parts of the CRS approach, and we therefore won't interpret them. We shall see in the next section the corresponding final CRS images, with much better quality.

Optimized attributes and stack

The same procedure as above was applied to clean the optimized attributes, but with different thresholds. As can be seen in Figure 14, which shows the results obtained for our same exemplary CMP, the best coherence is significantly lower, while the number of traces is much greater, than in the first CRS step. A convenient choice was to divide by a factor of 2 the previous coherence threshold. While this seems
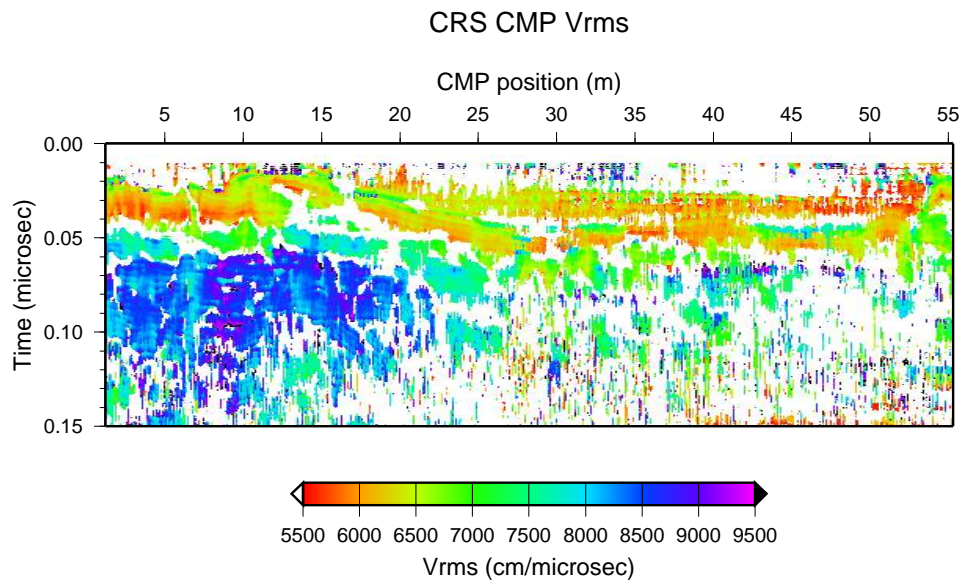
CRS CMP Vrms

CMP position (m)

Figure 12: Cleaned v_{rms} velocity field obtained by the automatic CMP step of the CRS method

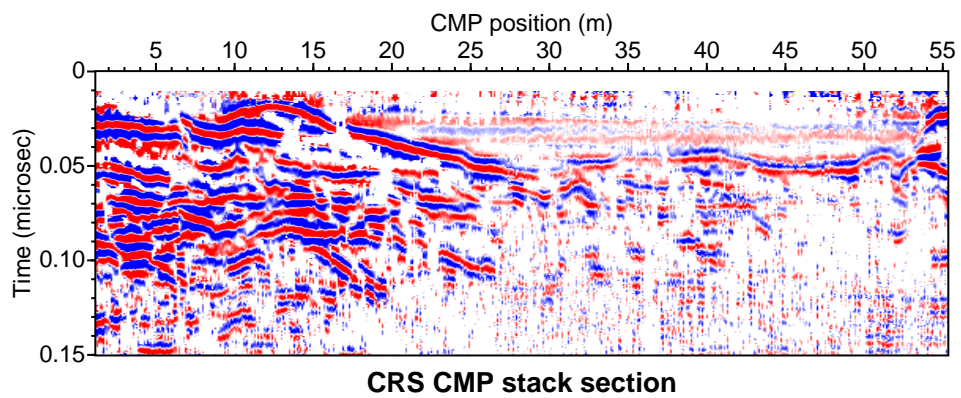CMP position (m)

CRS CMP stack section

Figure 13: Cleaned stack section obtained by the automatic CMP step of the CRS method
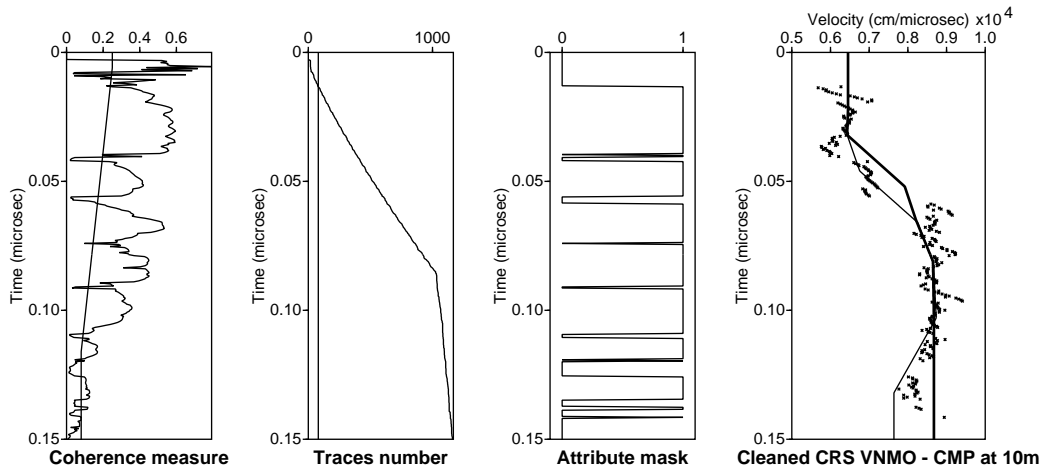
Figure 14: Same as Figure 11, for the optimized CRS attributes. Note that the coherency level is lower than for the automatic CMP attributes, so the threshold values are reduced by a factor 2

surprising since the parameters were optimized for best coherence, it should be recalled that the first CRS step is restricted to the CMP gather, with much less traces than the CRS supergather, so a strict comparison is not easy. However, the optimization step is improving coherence from the so-called *initial stack* CRS step (see above). Concerning the number of traces, as the minimal mid-point aperture includes 15 CMP on both sides of the center point, we fix at 90 the minimum number of traces within the semi-elliptical aperture. It can be seen in Figure 14 that CRS is conducting search and stack operations with up to about 1000 traces, instead of 28 for the classical NMO method.

An interesting feature appears at the inspection of the cleaned optimized v_{NMO} law obtained for our exemplary CMP (Figure 14, right). While both initial NMO manually picked or CRS automatically picked CMP coherence maxima lead to a physically impossible low velocity for time 0.13 microsec, the optimized v_{NMO} reveal a much more reasonable velocity, with a much reduced coherence value. Thus, it appears that for this event, the strong data coherence existing in the CMP gather for its small number of traces is not confirmed in the supergather with its very large number of traces. The CRS was thus able to filter out this anomaly event, which could otherwise has been mis-interpreted as a velocity anomaly. On the other hand, the case of the polarity inversion along the third reflection event is not better handled by the different CRS steps than by the NMO. The sole coherence/semblance criteria is clearly not adapted in this very special situation.

The final cleaned and optimized v_{NMO} and zero-offset (stacked) sections are shown in Figures 15 and 16. They appear on one side much more regular that their first CRS automatic CMP counterparts (Figures 12 and 13), but also reveals details not easily seen in their classical NMO counterparts (Figures 5 and 6). Although the CRS method is often thought as inducing a smoothing of the subsurface due to its use of supergathers, it appears here that it can recover very small-scale features, in particular when considering the v_{NMO} velocity field. It is still more impressive when compared with the classical NMO velocity field, which is over-smoothed due to its final interpolation step. However, it exists in the CRS velocity field too much high frequency variations, so that a direct conversion to interval velocities through the familiar Dix algorithm is not yet possible. We shall therefore conduct in the next section a regularization process of this velocity field.

CRS v_{NMO} **regularization**

The familiar Dix algorithm for inverting measured v_{rms} velocities into interval velocities v_{int} is long known to be unstable. Any small change of the v_{rms} value along the time axis can lead to a strong variation in the v_{int} value, so that physically impossible velocities are obtained. Therefore, this part of the work is
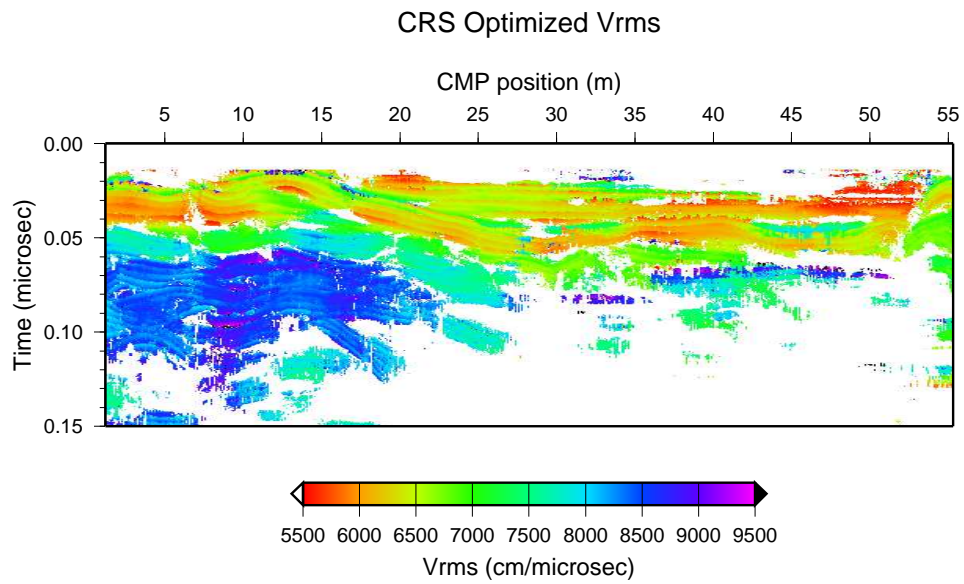
CRS Optimized Vrms

Figure 15: Cleaned v_{rms} velocity field obtained after the optimization step of the CRS method

CRS Opt stack section
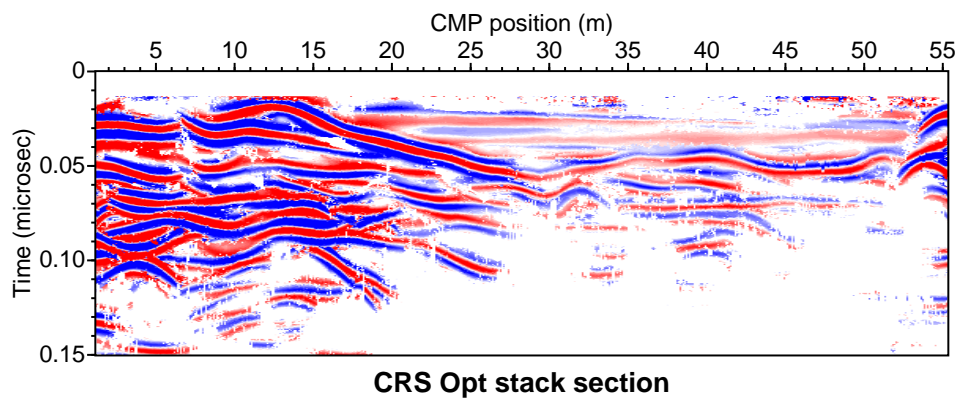
Figure 16: Cleaned stack section obtained after the optimization step of the CRS method
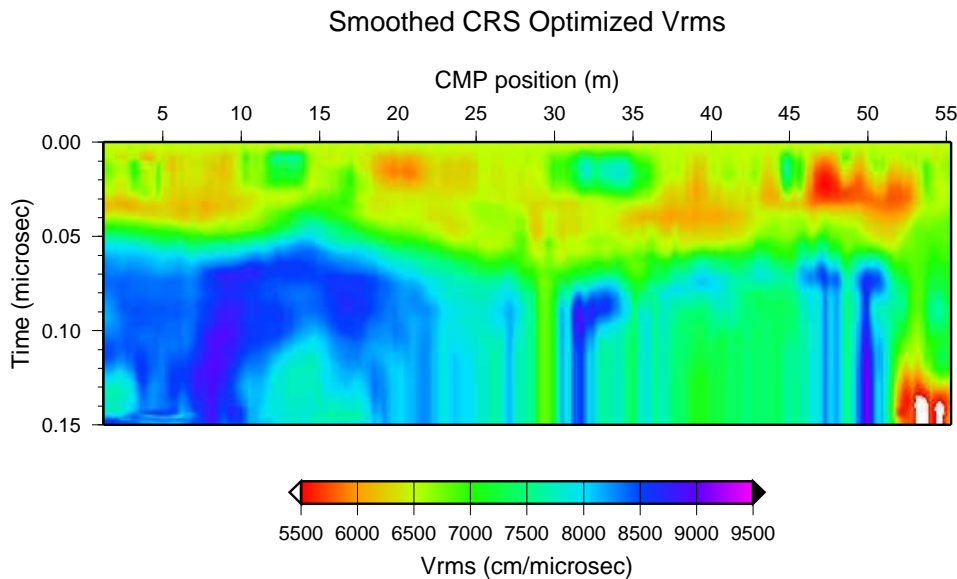
Smoothed CRS Optimized Vrms

Figure 17: Smoothed CRS $v_{\rm rms}$ velocity field

quite interesting to assess the quality of the CRS velocity determination. As already discussed above, even with the classical NMO approach which involves sparse velocity determinations and a large amount of interpolation, and which leads to a very smooth $v_{\rm rms}$ velocity field (Figure 5), we encountered that difficulty. For the CRS case, the situation could be much worse since for each CMP supergather, there is an independent $v_{\rm rms}$ attribute determination for each time sample. On the other hand, as there is a large overlap between neighboring supergathers, we can expect that the velocity determinations are correlated from trace to trace.

The regularization process we designed here includes several steps:

- Outliers elimination: the CRS coherence optimization lead in a few instances to anomalous velocity values, which survive to the cleaning process described above. In our cases, $v_{\rm rms}$ velocity lower than 5500 cm/microsec or higher than 9500 cm/microsec were considered as anomalous, and therefore blanked out. It concerns less than 1% of the CRS $v_{\rm rms}$ determinations.

- Interpolation of missing values: after the cleaning phase and the outliers elimination, there exists a fair amount of time samples for which there are no velocity determination available. To overcome this situation, it is a natural choice to interpolate along the time axis the missing values. We choose a simple linear interpolation to avoid the generation of unwanted oscillations. The CRS constant subsurface velocity was also affected to the upper part of each velocity trace (in the mute zone). Furthermore, the last available velocity sample was extrapolated to the end of the time axis. In this manner, we generate a velocity field which covers fully the investigated domain, as in the classical NMO approach.

- Smoothing along the vertical time axis: This point is essential due to the instability of the inversion process, as stated above. If we examine the optimized $v_{\rm rms}$ determinations for the exemplary CMP (Figure 14), it appears that the values are somewhat dispersed around a slowly varying general trend.

This high-frequency dispersion, although of moderate amplitude, cannot physically be associated with interval velocity fluctuations, since the v_{rms} definition by itself implies a too strong smoothing. We believe that this dispersion is rather linked to the coherency optimization of the CRS method, and that we have to get rid of it before going to a physical interpretation. To achieve this, we used for each CMP position a moving time-window average, with a width of 20ns that we have adjusted by trial and error, until we find that the high-frequency dispersion had vanished and the overall trend was recovered.

- Smoothing along the horizontal mid-point axis: the final step was a slight smoothing along the mid-point axis, within a radius of three mid-point interval, to improve the lateral consistency of the v_{rms} velocity field.

After the whole process, we obtained the smoothed CRS optimized v_{rms} section shown in Figure 17. It presents most of the low-frequency characteristics of the cleaned section of 15, but with a full domain coverage and a limited range of velocities. This is the section that will be converted to interval velocities in the next section. Note however that the lower right part of the section is very poorly constrained by available velocity determination.

Other regularization processes are also investigated as, for example, the stochastic reconstruction using a sequential Gaussian simulation (SGS) algorithm (see, e.g., Bleiner et al., 2000), based on correlation length determination using semi-variograms. They have certainly the potential to better fill the holes of the section, but they will not replace the smoothing part of the procedure, which will remain necessary.

VELOCITY MODELS EVALUATION

NMO-CRS comparison

Figures 5 and 17 are directly comparable, since they represent the same information, at the same level of the processing. It can be observed that the values are in general agreement, as well as the overall organization. However, thanks to the automated computation, the last (CRS) presents much more detailed variations of the velocity field, so we can hope that more useful geophysical information could be recovered. Once again, this will hold only if the interval velocity inversion can be achieved.

Interval velocity fields

The interval velocity sections obtained from both NMO and CRS v_{rms} sections are shown in Figures 18 and 19. Except for a few values which exceeds the shown velocity range, both sections present acceptable velocity values, and a reasonable general organization. However, it appears some slight anomalies, in yellow-red, with velocities lower than 5000 cm/microsec that can be considered as improbable. Otherwise, most of both sections present middle to high velocity that can are physically meaningful, given the known soil context. It should be noted that most unrealistic values from the CRS section are restricted in the lower right area which is not well constrained by the available data.

The vertical and lateral consistency of the velocity fluctuations seems much better in the CRS section, especially in the left part where the data are the most abundant and well determined. Furthermore, the overall organization of this same section has much better relationships with the independent electrical resistivity section (Figure 3), which also presents anomalies in the same depth range, and with local extrema in the same mid-point position (10m, 33m, 51m). The same cannot be stated for the NMO velocity section. It seems therefore that the CRS section can be much more easily correlated with other available geophysical evidences, and that is precisely what we need to achieve the targeted ground-water characterizations.

Ground-water properties

From both NMO and CRS derived velocity fields and the electrical resistivity field described previously, we have computed the water content and the fluid conductivity, following the method given in Garambois et al. (2002). The corresponding images are shown in Figure 20. It should be noted that the lower right parts of these images are very speculative, since no reliable velocity estimations have been possible here, neither by the NMO or CRS methods.
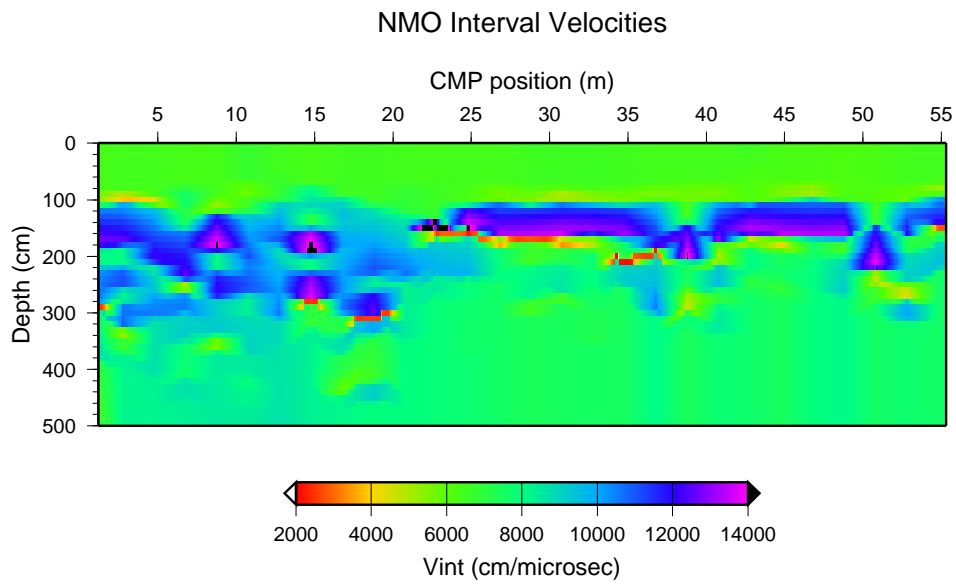
NMO Interval Velocities

CMP position (m)

Figure 18: Final interval velocity field obtained by the NMO method

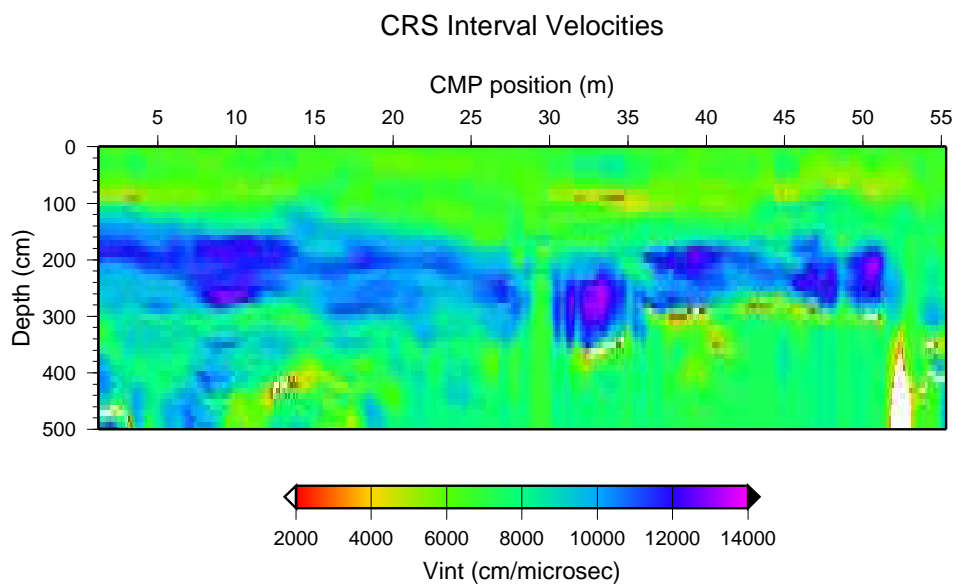## CRS Interval Velocities

CMP position (m)

Figure 19: Final interval velocity field obtained by the CRS method

It can be seen form this figure that once again, the CRS ground-water properties seem much more physically reasonnable than their NMO counterparts. This is specially true for the fluid conductivity that show anomalously high values in a significant part of the section for NMO, while the CRS reveals well-defined progressive high conductivity anomalies, which could correspond either to high clay content or high solution concentration. Only the persistance in time of such anomalies could help in resolve that final ambiguity, and it seems to us that the automated CRS approach will be much more helpful to obtain comparables images for different acquisition dates.

CONCLUSIONS

By means of a GPR real data example, we have examined the ability of the CRS to estimate rms-velocities that can be further inverted to a meaningful interval velocity field. Our results have shown that, apart from simple adjustments concerning scales and units, the CRS method very well extends its original use in seismics to the case of electromagnetic wave measurements. The comparison of the velocity analysis on the GPR dataset, conducted on the one hand by means of the classical NMO method and on the other hand by means of the CRS method, demonstrate that CRS method delivers a clearer and more detailed rms-velocity field than the NMO method in most parts of the section. One reason for this is that the CRS method uses much more traces during the velocity analysis as it takes advantage of the multi-parameter moveout surfaces as opposed to the single-parameter moveout curves of the NMO method. The inherent stretch effect of the NMO method, which does not occur in the CRS method, even enhance this.

The inverted interval velocity field of the CRS method looks in most parts physically more consistent than the interval velocity field inverted from the NMO method. The correlation of anomalies of the CRS interval velocity field and the electrical resistivity section confirms this fact. Therefore, the CRS velocity field in combination with electrical measurement seems to be more suitable for the evaluation of ground-water properties than the conventional NMO velocity field.

The CRS method at its current stage of implementation can be used as a black box processing tool. However, well-chosen input parameters, mainly with respect to the apertures, and right interpretation of the obtained attributes to get good results are mandatory—such as in the NMO processing. Therefore, hints for the determination of the best aperture values as well as further processing steps needed to receive the presented results have been discussed in detail.

ACKNOWLEDGEMENTS

REFERENCES

Biloti, R., Santos, L., and Tygel, M. (2002). Multiparametric traveltime inversion. *Stud. geophysica et geodaetica*, 46:177–192.

Bleiner, C., Perseval, P., Rambert, F., Renard, D., and Touffait, Y. (2000). *Isatis Software Manual V4.05*. Geovariances & Ecole des Mines de Paris.

Duveneck, E. and Hubral, P. (2002). Tomographic velocity inversion using kinematic wavefield attributes. In *Extended Abstracts*. 72nd Annual Internat. Mtg., Soc. Expl. Geophys. Session IT 2.3.

Garambois, S., Sénéchal, P., and Perroud, H. (2002). On the use of combined geophysical methods to assess water content and water conductivity of near-surface formations. *J. of Hydrology*, 259:32–48.

Höcht, G., de Bazelaire, E., Majer, P., and Hubral, P. (1999). Seismics and optics: hyperbolae and curvatures. *J. Appl. Geoph.*, 42(3,4):261–281.

Hubral, P. (1983). Computing true amplitude reflections in a laterally inhomogeneous earth. *Geophysics*, 48(8):1051–1062.
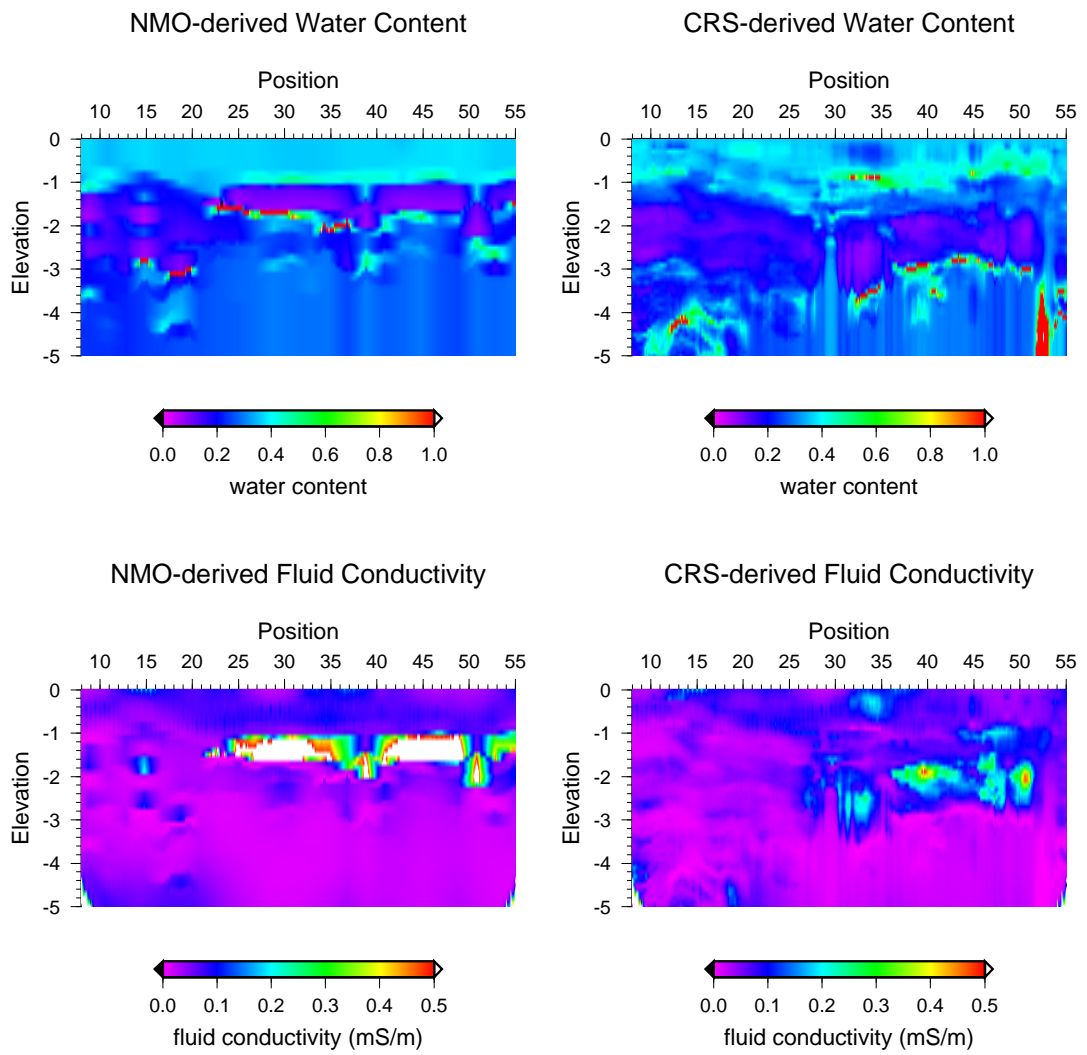
NMO-derived Water Content

CRS-derived Water Content

NMO-derived Fluid Conductivity

CRS-derived Fluid Conductivity

Figure 20: Compared ground-water properties derived from both NMO and CRS analyses

Hubral, P., editor (1999). *Macro-model independent seismic reflection imaging*, volume 42. J. Appl. Geophys.

Jäger, R., Mann, J., Höcht, G., and Hub ral, P. (2001). Common-reflection-surface stack: Image and attributes. *Geophysics*, 66(1):97–109.

Loke, M. and Barker, R. (1996). Rapid least-squares inversion of apparent resistivity pseudosections using a quasi-newton method. *Geophys. Prospect.*, 44:131–152.

Mann, J. (2002). *Extensions and applications of the Common-Reflection-Surface Stack Method*. Logos Verlag, Berlin.

Neidell, N. S. and Taner, M. T. (1971). Semblance and other coherency measures for multichannel data. *Geophysics*, 36(3):482–497.

Tygel, M., Müller, T., Hubral, P., and Schleicher, J. (1997). Eigenwave based multiparameter traveltime expansions. In *Expanded Abstracts*, pages 1770–1773. 67th Annual Internat. Mtg., Soc. Expl. Geophys.

Tygel, M., Schleicher, J., and Hubral, P. (1998). 2.5D kirchhoff MZO in laterally inhomogeneous media. *Geophysics*, 63:557–573.

Yilmaz, O. (2000). *Seismic Data Analysis*, volume 1, pages 1–1000. Soc. of Expl. Geophys.